



Computational comparison of conventional and inverted organic photovoltaic performance parameters with varying metal electrode surface workfunction

Christopher E. Petoukhoff^a, Divya K. Vijapurapu^a, Deirdre M. O'Carroll^{a,b,*}

^a Department of Materials Science and Engineering, Rutgers University 607 Taylor Road, Piscataway, NJ 08854, USA

^b Department of Chemistry and Chemical Biology, Rutgers University 610 Taylor Road, Piscataway, NJ 08854, USA

ARTICLE INFO

Article history:

Received 5 August 2013

Received in revised form

25 September 2013

Accepted 27 September 2013

Available online 1 November 2013

Keywords:

Inverted device

Computational methods

Metal electrode workfunctions

Bulk heterojunction organic photovoltaics

Performance parameters

ABSTRACT

Inverted polymer-based bulk-heterojunction organic photovoltaic (BHJ-OPV) device designs have enabled a breakthrough in operational lifetime through use of stable electrode materials. To date, there have not been systematic performance parameter comparisons between conventional and inverted devices that consider a range of different metal electrodes and presence of native metal oxides at the organic-metal interface. Here, we systematically compute optical and electronic performance parameters for both conventional and inverted BHJ-OPV devices for 15 different electrode types covering a range of workfunctions. We quantitatively demonstrate that (1) high-workfunction metal electrodes (Au, Pd, Ni) are ideal for high-efficiency inverted device performance; and (2) native metal oxide on metal electrodes (e.g., CuO/Cu, Ag₂O/Ag, NiO/Ni), which dramatically reduce conventional device efficiencies, can result in highly efficient inverted BHJ-OPV devices (efficiency of up to 6.7% for the P3HT:PCBM system). This work is an important advance over prior studies as it predicts the electrode materials and configurations that can lead to both high efficiency and high stability BHJ-OPV devices.

© 2013 Elsevier B.V. All rights reserved.

1. Introduction

In conventional bulk-heterojunction organic photovoltaic (BHJ-OPV) devices, the organic active layer is sandwiched between a low-workfunction metallic cathode (or electron collector) and a higher workfunction transparent anode (or hole collector, Fig. 1a). In recent years, a number of studies have demonstrated that low workfunction metallic cathodes are a primary contributor to device performance degradation for conventional BHJ-OPVs left in air [1–5]. In particular, degradation arises since, as metals oxidize or age, their workfunction increases (i.e., many have *p*-type semiconductor characteristics) [1,2,6–8], making them less effective electron collectors, which results in a marked reduction in the open-circuit voltage over time [7]. In inverted BHJ-OPVs, the polarity of the device is reversed: the metal acts as the anode and the transparent electrode acts as the cathode (Fig. 1a), usually through the use of high workfunction metals and/or the incorporation of appropriate transport layers. Thus, device degradation due to electrode oxidation is circumvented in inverted devices by

the use of metals as anodes, where the formation of a *p*-type metal oxide can allow for more effective hole collection. While low workfunction metals have conventionally been chosen to match the lowest unoccupied molecular orbital (LUMO) (~4 eV) of the electron acceptor (typically a fullerene derivative such as phenyl-C₆₁-butyric acid methyl ester, PCBM) [9–13], for inverted devices, the metal workfunction must match the highest occupied molecular orbital (HOMO) (~5 eV) of the electron donor (typically, poly(3-hexylthiophene), P3HT) [14–20]. As a result, inverted device designs have been shown to be substantially more air-stable than their conventional counterparts [1,2,5,21]. A secondary benefit of the inverted design is the elimination of poly(3,4-ethylenedioxythiophene):poly(styrenesulfonate) (PEDOT:PSS) layers, which are widely used in organic optoelectronics to improve the electrical properties of the anode [22–24], but are known to be corrosive to the transparent electrode [24,25].

Although the operational lifetimes of inverted BHJ-OPVs have been dramatically improved over conventional BHJ-OPVs [1,2,5,21], especially when left in air, the efficiency of inverted BHJ-OPVs has typically remained lower than that of comparable conventional devices – inverted devices based on a P3HT:PCBM blend typically reach ~3–4% efficiency [2,15,17–21,26–31] whereas the efficiency of conventional devices based on the same blend can reach 4–5% [10,32–37]. Although there have been many studies focused on optimizing the device structure of conventional

* Corresponding author at: Department of Materials Science and Engineering, Rutgers University 607 Taylor Road, Piscataway, NJ 08854, USA. Tel.: +1 848 445 1496.

E-mail addresses: c.petoukhoff@rutgers.edu (C.E. Petoukhoff),

divyavijapurapu@gmail.com (D.K. Vijapurapu),

ocarroll@rutgers.edu (D.M. O'Carroll).

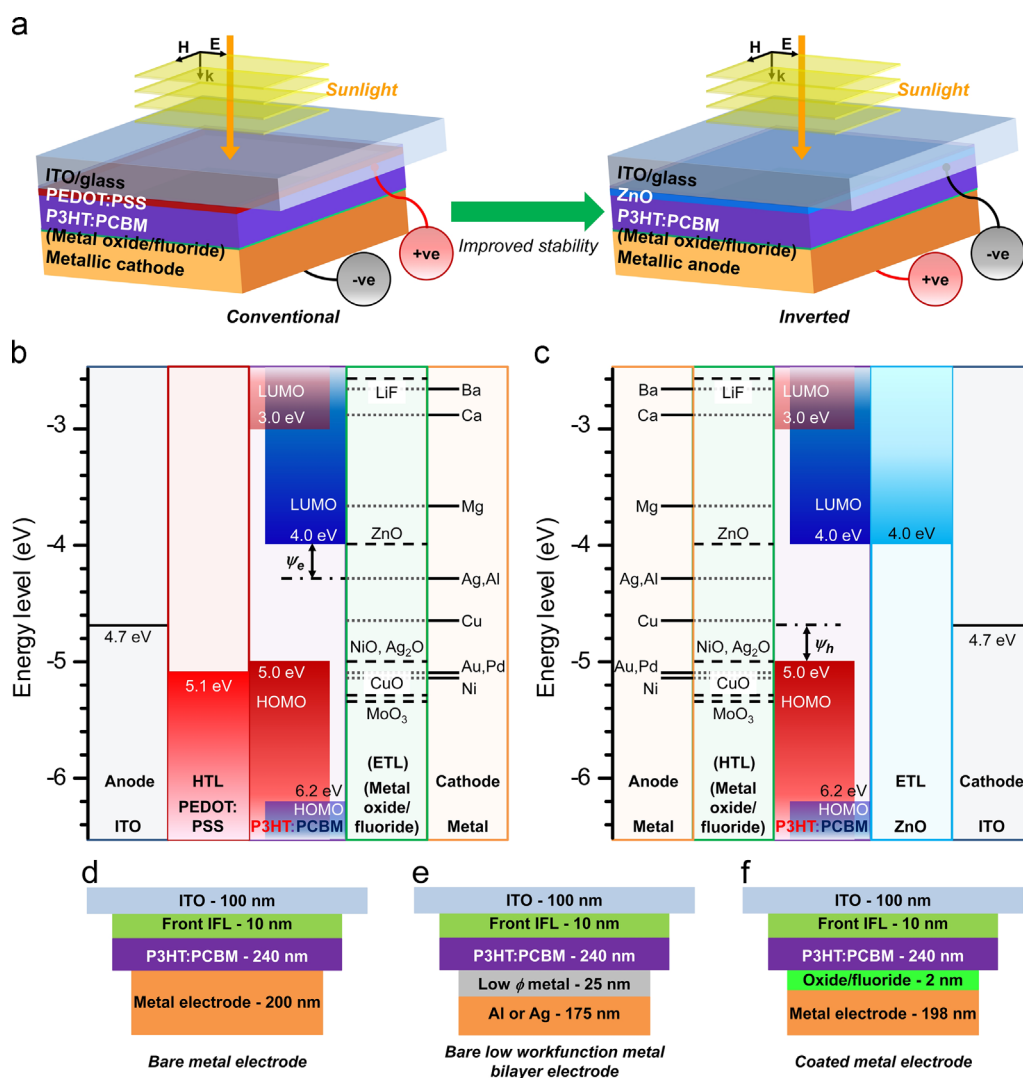


Fig. 1. (a) Schematic illustrating the different configurations for the BHJ-OPV devices studied here: conventional devices (left) and inverted devices (right) which may lead to improved BHJ-OPV device operational lifetime. A metal oxide/fluoride layer was present in 6 of the electrodes studied, but not present in the studies involving bare metal electrodes. (b)–(c) Energy level diagrams (flat-band conditions) for the corresponding (b), conventional and (c), inverted devices (magnitude of the energy levels is shown). The range of metals and metal oxides studied and their associated workfunctions are: LiF (2.6 eV) [60]; Ba (2.7 eV) [61]; Ca (2.87 eV) [61]; Mg (3.66 eV) [61]; ZnO (4.0 eV, see below); Ag (4.26 eV) [61]; Al (4.28 eV) [61]; Cu (4.65 eV) [61]; NiO (5.0 eV) [36,62]; Ag₂O (5.0 eV) [6,91,63–65]; Au (5.1 eV) [61]; Ni (5.15 eV) [61]; CuO (5.3 eV) [66,67]; MoO₃ (5.35 eV) [31,45,68–71] (data is given for polycrystalline materials). Note that although the workfunction of ZnO is typically cited between 4.1 and 4.4 eV [17,30,46,69,72–74], it is known to form an ohmic contact to PCBM [46,75], potentially due to formation of an interface dipole [75]. Other energy level data was obtained/averaged from the following references: ITO (4.7 eV) [36,43,45,68,69,76]; PEDOT:PSS (5.1 eV) [31,36,43,68,77]; P3HT HOMO (5.0 eV) [12,21,30,31,36,47,68,76,78–82]; PCBM LUMO (4.0 eV) [12,17,21,30,31,36,47,68,75,76,78–82].

BHJ-OPVs [9,12,32–36,38–42], there have been fewer studies to date where the device structure of inverted BHJ-OPVs has been optimized [2,16,19,28,29,43–46]. In one study by Schumann et al., inverted P3HT:PCBM devices consisting of electrodeposited ZnO as the electron transport layer (ETL) and WO_x-coated Al as the hole transport layer (HTL)-coated anode reached an efficiency of ~4.8% [46]. In another study by Hau et al., the optimized thickness and blend ratio for an inverted device consisting of ZnO prepared by the sol-gel method resulted with inverted device efficiency (~3.5%) exceeding that of a similarly fabricated conventional device (~2.4%, consisting of PEDOT:PSS as the HTL and LiF/Al as the ETL-coated cathode) [2]. A similar active layer blend ratio optimization was performed for a different layer morphology (a low bandgap polymer blended with PC₇₁BM), in which the ideal blend ratio for the inverted configuration was different than that of the conventional configuration, and the optimized inverted device efficiency (5.97%) exceeded that of a similarly fabricated

conventional device (5.41%), but was still lower than that of the optimized conventional device efficiency (6.24%) [44]. Further inverted BHJ-OPV device optimization is necessary in order to achieve device efficiencies that can perform as well as, or better than, comparable conventional devices.

There have been a number of studies comparing the performance of BHJ-OPVs using different metal cathodes in a conventional configuration [9,39–41] and different metal anodes in an inverted configuration [16]. Hadipour et al. recently compared, experimentally and computationally, the performance parameters of BHJ-OPVs incorporating different interfacial layers (IFLs), including the low workfunction metal, Ca [38]. In their study, the authors suggested that many low workfunction metals have large parasitic optical absorption, and that their elimination can further improve device efficiency [38]. However, while all of these studies have considered a range of metal workfunctions, there has not yet been a systematic study comparing the performance

parameters of BHJ-OPVs consisting of a range of metallic electrodes, both bare (no metal oxide) and coated with a native metal oxide, for both conventional and inverted devices. Furthermore, computational analysis of conventional BHJ-OPVs has greatly aided our understanding of the limits to device efficiency [11,12,37,38,47–54], and although there have been many experimental studies showing that high workfunction metals are beneficial for inverted BHJ-OPV device performance [1,14,17,20,55–57], this type of systematic study directly comparing inverted to conventional BHJ-OPVs for a variety of different bare and coated metal electrodes has not yet been explored computationally.

Here we computationally compare the performance of nine different bare metal and six metal oxide/fluoride-coated metal electrodes with a range of surface workfunctions in both inverted and conventional device configurations to identify the most suitable metal (either with or without an oxide/fluoride coating) in terms of both optical and electronic properties. We quantify the open-circuit voltage (V_{oc}) and fill factor (FF) for conventional and inverted devices for two different organic-metal interfacial interaction conditions: (1) assuming a large interface dipole between the metal and the organic layers (e.g., in the case of a strong interaction between the metal and organic layer, such as for chemisorption) [9,58,59]; and (2) assuming no interface dipole between the metal and the organic layers (e.g., in the case of a very weak interaction between the metal and organic layer, such as in physisorption) [41,58]. We show that the open-circuit voltage of conventional devices is optimal for low workfunction metals, while that of inverted devices is optimal for more air-stable, high workfunction metals. Additionally, we prove that inverted BHJ-OPVs can theoretically outperform conventional devices in terms of their short-circuit current densities (J_{sc}) due to the optical properties of the IFLs. The presence of an ultrathin (2 nm) metal oxide/fluoride coating does not significantly affect the J_{sc} based on our optical calculations, but markedly improves V_{oc} (electronic calculations). Finally, we demonstrate that native metal oxides are desirable for inverted device performance but detrimental to conventional device performance by calculating the total power conversion efficiency (η_p) for all device configurations and electrode types studied here.

2. Performance parameter calculations

2.1. Device setup

Fig. 1(a) shows general schematics of the different device configurations considered in this theoretical work. For typical conventional BHJ-OPV devices, indium-tin oxide (ITO) serves as the transparent anode, PEDOT:PSS serves as the HTL, and P3HT blended with PCBM is used as the active layer [32–35]. Although more efficient active layer morphologies have been identified (e.g., PCDTBT:PC₇₀BM [77], PTB7:PC₇₀BM [45]), the P3HT:PCBM blend system has been extensively studied [9,12,32–36,38–42] and is used as a model system for studying changes to the BHJ-OPV device structure other than the active layer [1,16,38–40,46]. A metal cathode, with or without a metal oxide or fluoride ETL, completes the device stack. For the inverted configuration, the bare or HTL-coated metal electrode serves as the anode and, typically, ZnO replaces PEDOT:PSS as the ETL [17,30,46], making ITO the cathode. In addition to the conventional and inverted device configurations defined above, we studied three possible cases at the metal electrodes defined as: (1) bare metal electrode (Fig. 1(d)); (2) bare low workfunction metal bilayer electrode (Fig. 1(e)); and (3) metal oxide/fluoride-coated metal electrode (Fig. 1(f)). The 6 bare metal electrodes studied were Ag, Al, Cu, Au,

Pd, and Ni; the 3 bare low workfunction metal bilayer electrodes studied were Ba/Al, Ca/Al, and Mg/Ag; all 9 of these metal electrode types will be referred to as the bare metal electrodes unless otherwise noted. The 6 coated metal electrodes studied were LiF/Al and ZnO/Al as *n*-type coatings; NiO/Ni, Ag₂O/Ag, CuO/Cu as *p*-type native metal oxide coatings, and MoO₃/Al as a standard *p*-type coating.

Fig. 1(d)–(f) also show the thicknesses of each of the layers employed in this computational study. For each electrode configuration, the thickness of the ITO was 100 nm [9], and the total metal electrode thickness was kept at 200 nm, ensuring that it was optically thick [83]. The thickness of the front IFLs (here defined as the HTL PEDOT:PSS for the conventional devices and the ETL ZnO for the inverted devices) and that of the P3HT:PCBM layers were optimized to be 10 nm and 240 nm, respectively (see Section 3.3 and Supporting information (SI) Fig. S1). For bare metals, the metal thickness was 200 nm; for the bare low workfunction bilayer metal electrodes, 25 nm of the low workfunction metal was supported by 175 nm of Al (for Ba and Ca) or Ag (for Mg) in keeping with typical experiments involving these metals in BHJ-OPVs [16,38–40]. For the coated metal electrodes, the thickness of the oxide/fluoride was 2 nm, and the metal was 198 nm. The thickness of the coating was chosen to modify the electrode workfunctions [6,36,84] without significantly changing the optical properties of the electrode. It should be noted that the thickness of LiF is typically ideal around 0.6 nm [85,86], but to minimize optical differences due to thickness changes, all of the coatings were kept at a constant thickness.

Fig. 1(b),(c) show energy level diagrams for both conventional and inverted device configurations, respectively. It was assumed that ohmic contacts occurred at the anode of the conventional device and the cathode of the inverted device, i.e., PEDOT:PSS was used as the HTL [11,24] and ZnO was used as the ETL [11,46,75] of the conventional and inverted devices, respectively. For conventional devices, metals and *n*-type coatings with workfunctions equal to or smaller in magnitude than the LUMO energy of PCBM are expected to form ohmic contacts at the cathode [9,11] (see Section 2.2). LiF and ZnO have been extensively studied for conventional BHJ-OPVs, and are known to form ohmic contacts to PCBM (see Section 2.2) [11,46,75,85,86]. Although the workfunction of ZnO is typically cited between 4.1 and 4.4 eV [46,75], it is expected to have a large interface dipole that reduces the energetic offset between the LUMO of PCBM and the workfunction of ZnO to nearly zero [75]; thus the workfunction of ZnO is taken to be equivalent to the LUMO of PCBM (4.0 eV). Metals or metal oxides with workfunctions larger in magnitude than the LUMO of PCBM can introduce an energy loss for electrons, ψ_e , collected from PCBM, which has previously been referred to as a barrier to electron injection [9,41], but barriers should not exist for an electron being collected by a high workfunction electrode [48]. For inverted devices, metals and *p*-type metal oxides with workfunctions equal to or larger in magnitude than the HOMO energy of P3HT are expected to form ohmic contacts at the anode [80] (see Section 2.2), whereas metals or metal oxides with workfunctions smaller in magnitude can introduce an energy loss for holes, ψ_h , from P3HT. Native *p*-type metal oxide formation was studied for 3 different metals – Ag₂O/Ag, NiO/Ni, CuO/Cu. Oxides of Ag, Cu, and Ni have been shown to be of benefit to organic light emitting diodes (OLEDs) [6,8,64,84,87–91] as well as OPVs [7,36,65,92–93]. CaO has been shown to be detrimental to device performance by creating voids in the electrode [1], and so insulating native metal oxides (BaO, CaO, MgO, Al₂O₃) are not considered here, but are expected to degrade device performance in all cases. Au and Pd are not expected to spontaneously oxidize in air, so oxides of Au and Pd were also not considered here. For comparison, MoO₃/Al, which is a common anode for inverted BHJ-OPVs, was studied [29–31,43,45,68]. While the results presented here are purely computational, they can be used as design

criteria for future electrode selection for inverted and conventional BHJ-OPVs and are relevant to various methods of electrode deposition [94,95].

2.2. Open-circuit voltage calculation

The maximum attainable V_{oc} of a BHJ-OPV for a given donor–acceptor blend, $V_{oc,max}$, has been shown to be given by [12]:

$$V_{oc,max} = \frac{1}{q} (|E_{HOMO}^{donor}| - |E_{LUMO}^{acceptor}| - \Delta E) \quad (1)$$

where q is the elementary charge (in units of C), E_{HOMO}^{donor} is the HOMO energy level of the donor, $E_{LUMO}^{acceptor}$ is the LUMO energy level of the acceptor, and ΔE is an empirical factor equal to 0.3 eV for P3HT:PCBM. The physical significance of ΔE is still debated but is believed to be related either to the combination of the reverse dark current of the photodiode and the field-driven photocurrent in BHJ-OPVs [12], or the exciton binding energy [96]. For ohmic contacts at both the anode and cathode, the $V_{oc} = V_{oc,max}$ because there are no energy losses due to energy level mismatches. In the case of non-ohmic contacts, however, the V_{oc} is reduced by an amount proportional to the energy loss for electrons and/or holes, $\psi_{e/h}$, at the respective electrodes:

$$V_{oc} = \frac{1}{q} (|E_{HOMO}^{donor}| - |E_{LUMO}^{acceptor}| - \Delta E - S_c \psi_e - S_a \psi_h) \quad (2)$$

where $S_{c/a}$ are the slope parameters for the dependence of V_{oc} on cathode/anode workfunction. The slope parameter, S , is a measure of the strength of the interaction between the organic layer and the electrode. A strong interaction between the organic layer and the electrode usually occurs due to the formation of an interface dipole between the two layers, which is highly dependent on the identity of the two materials, the properties of their interface, and the method of depositing one material on the other [9,58,59,97]. For BHJ-OPV devices, the S -parameter typically represents the V_{oc} dependence on metal workfunction; however, S -parameters have also been defined for organic films on varying substrates, where the S -parameter represents the dependence of the effective workfunction of the organic-coated substrate on the workfunction of the bare substrate [59,98,99]. Both the S -parameter for devices and that for films are measures of the energy level alignment of the organic molecular orbitals and the underlying substrate Fermi level. The stronger the interface dipole, the lower the S -parameter value, which has been shown to be as small as 0.1 for non-ohmic contacts [9,58,97]. The typical metal-insulator-metal (MIM) model that has been used previously [41,42] to calculate V_{oc} assumes that there is no interface dipole formed, and that V_{oc} depends linearly on the metal workfunction, with an S -parameter of 1; this should occur in the case of vacuum-level alignment, or the Mott-Schottky limit [58,59,98,99]. In the case of ohmic contacts, it has been shown that there is no dependence of V_{oc} on metal workfunction, regardless of the workfunction of the metal [16,41,42], a process which has been referred to as ‘Fermi level pinning’. Therefore, in the pinning regime, the S -parameter is zero [16,58,59,98,99]. The S -parameter for non-ohmic contacts has been cited as 0.1 [9], 0.26 [42], 0.6 [16], and 1.0 [41,58,98,99]. The V_{oc} was thus calculated for an S -parameter of 1.0, which assumed no interface dipole formation [41,58,98,99], as well as for an S -parameter of 0.1, which assumed formation of a strong interface dipole [9,58,97] for non-ohmic contacts. For ohmic contacts, an S -parameter of 0 was used.

Ohmic contact occurs between the cathode and the n -type acceptor material when the magnitude of the workfunction of the cathode, ϕ_c , is less than or equal to $|E_{LUMO}^{acceptor}|$, due to Fermi level pinning [16,58,59,98,99], and $\psi_e = 0$. For non-ohmic contact between the cathode and the acceptor, $|\phi_c| > |E_{LUMO}^{acceptor}|$, there is

an energy loss for electrons at the cathode defined as:

$$\psi_e = |\phi_c| - |E_{LUMO}^{acceptor}| \quad (3)$$

(see Fig. 1(b)). For the case where the magnitude of the workfunction of the anode, ϕ_a , is greater than or equal to $|E_{HOMO}^{donor}|$, an ohmic contact is formed to the p -type donor material due to Fermi level pinning [16,58,59,98,99] and $\psi_h = 0$. For $|\phi_a| < |E_{HOMO}^{donor}|$ there is an energy loss for holes at the anode, which we define as:

$$\psi_h = |E_{HOMO}^{donor}| - |\phi_a| \quad (4)$$

(see Fig. 1(c)). The V_{oc} was then calculated assuming that $|E_{HOMO}^{donor}|$ of P3HT is 5.0 eV, $|E_{LUMO}^{acceptor}|$ of PCBM is 4.0 eV (see Fig. 1 for references), and ΔE for P3HT:PCBM is 0.3 eV [12].

2.3. Fill factor calculation

Analytical expressions for the fill factor have been proposed by Green in 1982 [100] and applied to BHJ-OPVs by Servaites et al. in 2009 [49]. Briefly, the ideal fill factor (FF_0) which assumes ideal shunt and series resistances (i.e., shunt resistance $\rightarrow \infty$; series resistance $\rightarrow 0$), was calculated as follows [49,100]:

$$FF_0 = \frac{v_{oc} - \ln(v_{oc} + 0.72)}{v_{oc} + 1} \quad (5)$$

where v_{oc} is the normalized open-circuit voltage defined as:

$$v_{oc} = V_{oc} \left(\frac{q}{n_d k_B T} \right) \quad (6)$$

where n_d is the diode ideality factor, k_B is the Boltzmann constant, and T is temperature. If non-zero series resistances are present, the series fill factor (FF_s) is calculated as [49,100]:

$$FF_s = FF_0 (1 - 1.1 r_s) + \frac{r_s^2}{5.4} \quad (7)$$

where r_s is the normalized series resistance defined as:

$$r_s = \frac{R_s}{V_{oc}/J_{sc}} \quad (8)$$

where R_s is the specific series resistance (in units of $\Omega \text{ cm}^2$). Finally, when finite shunt resistances are considered, the total fill factor (FF) was calculated as [49,100]:

$$FF = FF_s \left(1 - \frac{v_{oc} + 0.7 FF_s}{v_{oc} r_{sh}} \right) \quad (9)$$

where r_{sh} is the normalized shunt resistance defined as:

$$r_{sh} = \frac{R_{sh}}{V_{oc}/J_{sc}} \quad (10)$$

where R_{sh} is the specific shunt resistance (in units of $\Omega \text{ cm}^2$). Eqs. (5), (7), and (9) are accurate to less than a few percent for $v_{oc} > 10$ and $r_s + 1/r_{sh} < 0.4$ [100]. Values of n_d for P3HT:PCBM BHJ-OPVs were taken from the literature and averaged (See SI Table S8). R_s values were obtained for both P3HT:PCBM BHJ-OPV devices containing PEDOT:PSS hole transport layers (conventional) and ZnO electron transport layers (inverted) (See SI Table S8). Here, $n_d = 1.83$, $R_s = 4.51 \Omega \text{ cm}^2$ for conventional devices, $R_s = 5.36 \Omega \text{ cm}^2$ for inverted devices, and room temperature (300 K) operation was assumed. Shunt resistance values varied considerably in the literature, but according to Servaites et al., for well-optimized BHJ-OPVs, $R_{sh} = 1 \text{ M}\Omega \text{ cm}^2$ is a typical value [49]. Tabulated values of FF , FF_s , FF_0 , the normalized parameters, and literature values for the equivalent circuit parameters can be found in the SI.

2.4. Short-circuit current density calculation

The J_{sc} is related to the efficiency of absorption of photons by the active layer (optical properties), as well as the efficiencies of separation and transport of the electrons and holes to their respective electrodes (electrical properties). The J_{sc} depends on the external quantum efficiency, η_{EQE} , of the device as follows [11,101]:

$$J_{sc} = q \int_{\lambda} \eta_{EQE}(\lambda) N_{ph}(\lambda) d\lambda \quad (11)$$

where λ is the wavelength (in units of nm) and N_{ph} is the photon flux density of the AM 1.5 solar spectrum over the wavelength range of interest (in units of photons $\text{m}^{-2} \text{nm}^{-1} \text{s}^{-1}$) [11]. The η_{EQE} , which is defined as the ratio of the number of free carriers collected at the electrodes to the number of photons incident on the device, is determined by the product of the individual quantum efficiencies of each step of the conversion process of photons to electrons [10,11,13] (see SI, Fig. S2). Here, we approximate the η_{EQE} to be given by:

$$\eta_{EQE}(\lambda) \approx \eta_a(\lambda) \quad (12)$$

where η_a is the efficiency of photon absorption (see SI for details). By making this approximation, we have assumed that each photogenerated exciton has dissociated into free charge carriers, each of which have been collected at the respective electrode. While this effectively neglects the electrical transport aspects of the devices, e.g., by assuming an internal quantum efficiency (η_{IQE}) value of 100% (see Section 4.5 and SI for further discussion), there is not expected to be a notable change in the efficiency of charge transport within the active layer for devices having different metallic electrodes, particularly since the generation rate maxima are located in nearly the same spatial position of the active layer for each electrode (SI Fig. S3).

Further, since the calculations in this work were carried out on a discrete basis, the integral in Eq. (11) becomes a summation:

$$J_{sc} = q \sum_{\lambda} (\eta_a(\lambda) N_{ph}(\lambda) d\lambda) = q \sum_{\lambda} \left(\eta_a(\lambda) \frac{I_{solar}(\lambda)}{h\nu} d\lambda \right) \quad (13)$$

where the photon flux density has been evaluated as the power density of light from the AM 1.5 solar spectrum, I_{solar} (in units of $\text{W m}^{-2} \text{nm}^{-1}$) divided by the energy per incident photon ($h\nu$, where h is Planck's constant (in units of J s photon^{-1}) and ν is the frequency of light (in units of s^{-1})). From Eq. (13), it is clear that in order to calculate the J_{sc} of BHJ-OPV devices (assuming good electrical transport through the active layer), it is necessary to calculate η_a , the efficiency of photon absorption by the active layer.

The η_a is related to the power density absorbed in the active layer, I_{active} ($\text{W m}^{-2} \text{nm}^{-1}$), by dividing it by the incident power density, I_{solar} :

$$\eta_a = \frac{I_{active}(\lambda)}{I_{solar}(\lambda)} \quad (14)$$

where I_{active} is given by [51]:

$$I_{active}(\lambda) = \sum_z^{thickness} Q(z, \lambda) \cdot dz = \sum_z^{thickness} \alpha n I_{solar} \left| \frac{E(z, \lambda)}{E_0} \right|^2 \cdot dz \quad (15)$$

where Q is the thickness- and wavelength-dependent power absorbed by the active layer and is summed over the thickness of the active layer to determine the total power density absorbed by the active layer, α is the absorption coefficient of the active layer (in units of cm^{-1} , see Eq. (16)), n is the real part of the complex index of refraction, and $|E/E_0|^2$ is the normalized electric field intensity in the active layer. The absorption coefficient is

related to the imaginary part of the complex index of refraction, k [102]:

$$\alpha = \frac{4\pi k}{\lambda} \quad (16)$$

By inserting Eqs. (14) and (15) into (13), the J_{sc} can be expressed as:

$$J_{sc} = q \sum_{\lambda}^{solar \ thickness} \sum_z \left(\alpha n \left| \frac{E(z, \lambda)}{E_0} \right|^2 \frac{I_{solar}(\lambda)}{h\nu} dz d\lambda \right) \quad (17)$$

$$J_{sc} = q \sum_{\lambda}^{solar \ thickness} \sum_z \left(\frac{Q(z, \lambda)}{h\nu} dz d\lambda \right) \quad (18)$$

$$J_{sc} = q \sum_{\lambda}^{solar \ thickness} \sum_z (G(z, \lambda) dz d\lambda) \quad (19)$$

where G is the generation rate of excitons in the active layer and is equal to $Q/h\nu$, or the power absorbed by the active layer divided by the energy of an incident photon. As seen from Eq. (17), based on the assumptions made here, the J_{sc} is primarily determined by the optical constants (n and k) and the electric field intensity within the device. Due to the nature of thin films, there is coherent interference that occurs within each layer of the device, since the thickness of each layer is on the order of or less than the wavelength of light, so the electric field intensity will vary greatly with changing thickness of each layer (see Section 3.1 for method of calculating electric field intensity). As such, the thicknesses of ITO, the metal electrode, and the metal oxide coatings (when present) were fixed (see Section 2.1), but the thicknesses of the active layer and front IFL were optimized (see Section 3.3).

2.5. Efficiency calculation

The overall power conversion efficiency, η_p , was calculated from the performance parameters determined from the equations in Sections 2.2 - 2.4 using the following equation:

$$\eta_p = \frac{J_{sc} V_{oc} FF}{I_{solar}} \times 100\% \quad (20)$$

3. Computational methodology

3.1. Electric field calculations/simulation parameters

Full-field electromagnetic calculations were performed numerically using commercially available finite-difference time domain (FDTD) software [103] for all of the devices studied here (see SI Fig. S8). The FDTD method was preferred over the traditional transfer matrix (TM) method because, although the TM method is good for studying planar thin films, it cannot be used to study effects such as non-homogenous active layer morphologies [104–108], scattering from rough surfaces [109], or confinement of the electric field from nanophotonic structures [108–112]; however, we do not consider these factors in this study. Numerical techniques such as the FDTD method are useful for studying these structures, some of which are the subject of on-going work. In the simulations, plane wave excitation incident normal to the plane of the device was employed in all cases. Similar to the TM method, the FDTD method assumes that optical materials are non-magnetic (relative permeability, $\mu_r = 1$) such that the only necessary data to input into the software are the optical constants, n and k (or equivalently the dielectric function, $\epsilon = \epsilon_1 + i\epsilon_2$) of each material, and the dimensions of each layer and nanostructure. However, there are a number of simulation parameters that must be considered to ensure accurate results are achieved, e.g. the size

of the mesh, the properties of the source, and the boundary conditions. In order to verify the accuracy of the FDTD simulations, initial simulations were compared to results obtained using the TM calculations, which were shown to agree to within 1% (see SI Table S1 and Fig. S9).

The FDTD method cannot be used practically for nanometer-scale objects distributed on the macro or millimeter scale due to limited computational resources; it is primarily used for structures of nano- or micrometer size. As such, the glass substrate is not included in the device, but the background index through which the electromagnetic source initially propagates is set to that of SiO₂ glass ($n=1.52$). The final result is then corrected for reflective losses at the air–glass interface from multiple passes through the device stack by multiplying the numerically calculated electric field value by the transmission coefficient at the glass–ITO interface as calculated by the TM methods (see SI for further discussion on correcting for substrate effects).

The thickness of the remaining layers were set to the values described in Section 2.1. Each layer had a cross-sectional area that was ‘infinite’ in extent by defining appropriate boundary conditions; see below. The FDTD simulation region cross-sectional area was set to 20 nm × 20 nm (see SI, Fig. S8) with a depth of 1700 nm. The source was a plane wave pulse, with continuous wave normalization (CWN), a pulselength of 2.325 fs, wavelength range of 350–800 nm, and wavelength stepsize of 1 nm. The solar irradiance AM 1.5 spectrum was taken into consideration during post-simulation processing (see Eq. (17)). As such, the source had an amplitude of 1, phase of 0°, and the polar and azimuthal angles were both also set to 0° (normal incidence). The source propagated in the direction normal to the device (z) with the electric field vector (\mathbf{E}) polarized along the x direction and the magnetic field vector (\mathbf{H}) polarized along the y direction (see SI, Fig. S8 for orientation of the axes). The source was 1000 nm from the first layer of the device. A two-dimensional frequency-domain field and power monitor as well as a 2D refractive index monitor were included in the simulation (in the x – z plane at $y=0$). The geometries of these monitors were identical and chosen to agree with the polarization of the plane wave source; the monitors extended beyond the simulation region in the x and z directions. SI Fig. S8 shows the graphical user interface (GUI) representation of the simulation setup.

The boundary conditions of the simulation were as follows: anti-symmetric boundary conditions along the polarization direction of the \mathbf{E} -field (x), symmetric boundary conditions along the polarization of the \mathbf{H} -field (y), and perfectly matched layer (PML) boundary conditions along the direction of propagation (z) [103], with 12 PMLs. Symmetry was enabled on all boundaries, and the structure was extended through the PMLs. The simulation time was 1000 fs. The simulations had a mesh accuracy set to 8, with mesh refinement type set to conformal variant 1 [103]. A mesh override of $dx=dy=dz=0.9$ nm was set through the entire device. The simulations automatically shut-off when the normalized field intensity decays to less than 10^{-7} .

3.2. Optical constants

For the simulations, the wavelength-dependent complex index of refraction ($\tilde{n}=n+ik$) of each layer of the device (metal, active layer, interface layers, transparent conducting electrode, glass) were required. The optical constants (n and k) were obtained from: an index of refraction library compiled by Burkhardt et al. [52] for ITO, PEDOT:PSS, Al, and Ca; an online database [113] for Au, Cu, CuO, Ni, and Pd; the Handbook of Optical Constants (Palik), provided by Lumerical FDTD Solutions [103] for Ag; Monestier et al. [51] for P3HT-PCBM; Postava et al. [114] for ZnO; Gao et al. [115] for Ag₂O; Kumagai et al. [116] for NiO; Endriz et al. for Ba

[117]; Machorro et al. [118] for Mg; the Handbook of Chemistry and Physics [119] for LiF; and May et al. [120] for MoO₃. SiO₂ was assumed to have a constant n of 1.52 throughout the visible spectrum and a constant k of 0 in order for the TM calculations to match the FDTD calculations (in the latter the background index must be set to a constant value (1.52)). See SI Fig. S5 for plots of optical constants of all materials used in this study.

In order to simulate the electric field profile using Lumerical FDTD Solutions [103], the optical constants must be fit to a polynomial equation, which is optimized in the software itself. The input values into these fitting routines were 50 linearly spaced optical data points in the wavelength range of 350–800 nm. After the data were fitted, the polynomials were used in the software to obtain n and k at each wavelength between 350 and 800 nm (451 total wavelength points). This fitted discrete data was then exported from Lumerical to be used in the TM method calculations such that complex index of refraction of each layer was as similar as possible for the two methods of calculating the electric field profile were as similar as possible.

3.3. Thickness optimization

The front interface layer (PEDOT:PSS) and the active layer (P3HT:PCBM) for a conventional BHJ-OPV device were optimized by fixing the thicknesses of the other layers (as described in Section 2.1), and using a bare Al cathode, then performing FDTD simulations for 5 different PEDOT:PSS thicknesses (ranging from 10 to 50 nm, in 10 nm intervals), each having 12 different P3HT:PCBM thicknesses (ranging from 20 to 240 nm, in 20 nm intervals). The J_{sc} was calculated for each simulation and an oscillatory-type behavior was observed for changing P3HT:PCBM thickness, as observed for others in the literature [33,37,51,53,54]. See SI Fig. S1 for optimization plot. The optimized thicknesses of the PEDOT:PSS and P3HT:PCBM layers were 10 nm and 240 nm, respectively.

4. Results and discussion

4.1. Open-circuit voltage

Fig. 2 (top panel) shows the results of the calculations of V_{oc} for the 15 different electrode types studied here. Note that in the case of a p -type coating on the cathode as well as an n -type coating on the anode, the V_{oc} was assumed to be zero, since they should serve as effective electron and hole blocking layers, respectively [36,121]. The presence of strong interface dipoles (S_c or $S_a=0.1$ at the cathode or anode of the conventional or inverted devices, respectively), which may form for strongly interacting layers [58], reduced the energy loss for charge collection (ψ_e or ψ_h) at the respective electrodes, and increased V_{oc} . With optimized workfunctions (i.e., ohmic contacts at both the cathode and anode), maximum attainable open-circuit voltage ($V_{oc,max}$) values of 0.7 V were calculated for both conventional and inverted P3HT:PCBM BHJ-OPV devices (which is in good agreement with the design rules developed by Scharber et al. [12], assuming a LUMO energy for PCBM of 4.0 eV and a HOMO energy of P3HT of 5.0 eV [36,76]). For conventional devices, V_{oc} was negligible for $S_c=1$ when $|\phi_c| \geq |E_{LUMO}^{acceptor}| + qV_{oc,max}$, since the electron energy loss at the cathode exceeded the total V_{oc} (see Fig. 1(b)). For inverted devices, V_{oc} was also negligible for $S_a=1$ when $|\phi_a| \leq |E_{HOMO}^{donor}| - qV_{oc,max}$ again due to the hole energy loss at the anode (see Fig. 1(c)) exceeding the total V_{oc} . For conventional devices, with increasing metal electrode workfunction, the V_{oc} decreased from its maximum value to 0.585 V for $S_c=0.1$ and to 0 V for $S_c=1$ for the highest workfunction metals (Ni, Pd, Au). For inverted

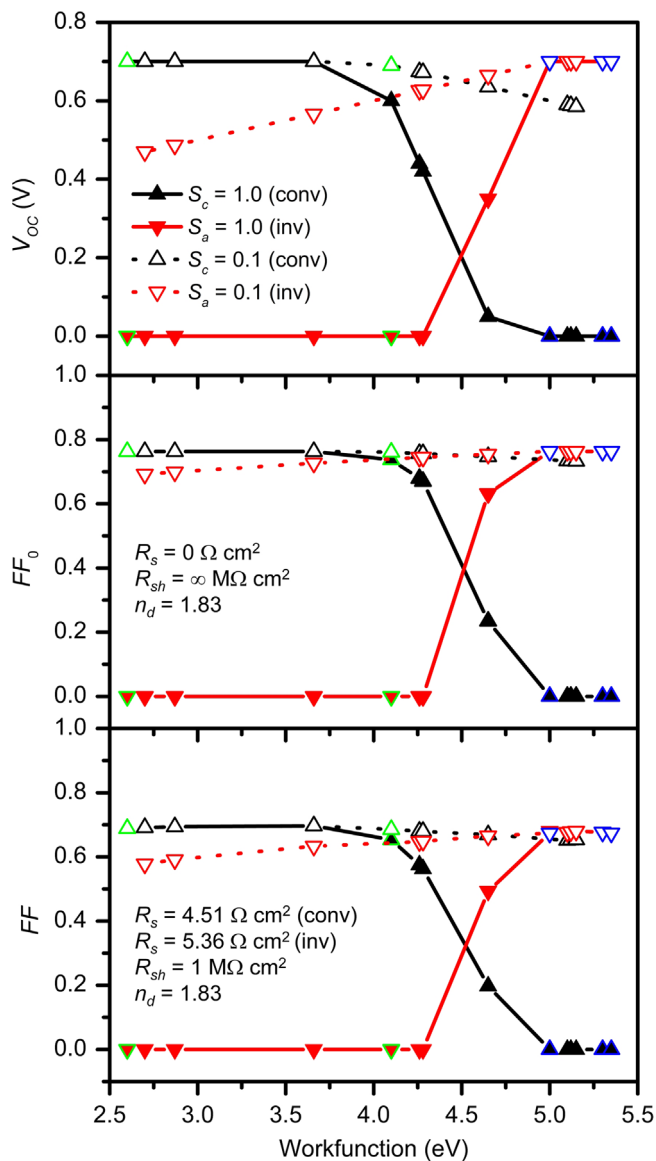


Fig. 2. Calculated V_{oc} (top panel), FF_0 (middle panel) and FF (bottom panel) as functions of increasing workfunction for the 9 bare metal and 6 coated metal electrodes studied. For inverted devices, calculations were performed for both a slope parameter, S_a , of 1.0 (for all bare and coated metal anodes; solid symbols) and S_a of 0.1 (for all bare metal and only p -type coated metal anodes; hollow symbols). For conventional devices, calculations were performed for both a slope parameter, S_c , of 1.0 (for all bare and coated metal cathodes; solid symbols) and S_c of 0.1 (for all bare metal and only n -type coated metal cathodes; hollow symbols). Symbols with blue outlines denote values calculated for p -type metal oxides and symbols with green outlines denote values calculated for the n -type metal oxide and fluoride. Equivalent circuit values used for the FF_0 and FF calculations are shown as insets in the middle and bottom panels, respectively. Note that for materials with identical workfunctions, their V_{oc} , FF_0 , and FF values are also identical.

devices, with increasing bare/coated metal electrode workfunction, the V_{oc} increased to its maximum value from 0.47 V for $S_a=0.1$ and from 0 for $S_a=1$ for the lowest workfunction bare metals (Ba/Al, Ca/Al, Mg/Ag). The best performing cathodes for the conventional configuration were composed of the unstable low workfunction metals (i.e., LiF/Al, Ba/Al, Ca/Al, and Mg/Al) and for the inverted configuration were anodes with native metal oxide coatings (i.e., Ag_2O/Ag , NiO/Ni , and CuO/Cu), the stable high workfunction metals (Au, Pd, and Ni) and the standard inverted BHJ-OPV anode (i.e., MoO_3/Al). Comparison of the V_{oc} calculations to experimental data will be provided in Section 4.5.

4.2. Fill factor

The FF showed the same trends as V_{oc} for both device configurations and the range of electrode materials studied (Fig. 2, middle and bottom panels), with maximum achievable values of 0.76 assuming no parasitic resistances (i.e., $R_s=0$, $R_{sh}=\infty$). For $V_{oc}=0$, the FF_0 according to Eq. (5) results in a value of 0.33 due to the limited accuracy of the fill factor calculation for $v_{oc} < 10$ (see Section 2.3 and SI Tables S4–S7 for v_{oc} values); however, a fill factor for $V_{oc}=0$ has no physical significance, so the FF_0 was set to 0 in these cases. Assuming no parasitic resistances, the maximum FF_0 was identical for the conventional and inverted devices. However, the more meaningful calculation incorporating parasitic resistances resulted in reduced FF values (Fig. 2, bottom panel), giving a maximum value for the FF of 0.70 for conventional devices and 0.68 for inverted devices. The main reason for this difference is the larger R_s for ZnO-based BHJ-OPVs ($5.36 \Omega \text{ cm}^2$) compared to PEDOT:PSS-based devices ($4.51 \Omega \text{ cm}^2$). If the R_s for inverted devices is set equal to or less than that of conventional devices, then the maximum FF for inverted devices can exceed that of conventional devices. Comparison of the FF calculations to experimental data will be provided in Section 4.5.

4.3. Optical absorption spectra and short-circuit current density

Calculations of the optical absorption and J_{sc} in the devices as a function of bare and coated metal electrode materials were performed to identify the electrodes with the most desirable optical response (i.e., low absorption loss) for the BHJ-OPV devices studied here. Fig. 3(a) and (b) show the calculated active layer absorption spectra for both conventional and inverted device configurations, respectively, for each of the 9 different bare metal electrodes. Since the coated metal electrodes showed very similar trends as their bare counterparts (within $\sim 10\%$ on average across the spectrum), the coated metal results are not shown in Fig. 3 (see SI, Fig. S4). It was observed that Ag and Al electrodes resulted in the largest overall absorption in the active layer, with $\sim 90\%$ of light absorbed between 380 and 610 nm. For Au, Cu, Ba/Al, Pd, Ni, Ca/Al, and Mg/Ag electrodes, active layer absorption ranged from $\sim 83\%$ to 90% between 350 and 550 nm for the conventional configuration. Between 550 nm and 610 nm, devices with Au, Cu, and Ba/Al electrodes absorbed between 80 and 85% of light in the active layer, but for Pd, Ni and Ca/Al electrodes, active-layer absorption dropped to $\sim 75\text{--}78\%$, and for Mg/Ag electrodes active-layer absorption dropped further to $\sim 65\text{--}85\%$. All active layer absorption dropped rapidly to $\sim 10\%$ from 610 to 660 nm, then continued to drop towards 0% at longer wavelengths. For all metals, the absorption onset in the active layer occurred at $655 \pm 5 \text{ nm}$. Conventional and inverted active layer absorption spectra showed similar trends, except for an additional dip in the inverted fractional absorption spectra in the range 350–380 nm arising as a result of interband absorption from the ZnO ETL (see SI, Fig. S5).

The fraction of light absorbed (i.e., parasitic absorption) by the metal electrode for both the conventional and inverted configurations is shown in Fig. 3(c) and (d), respectively, for the 9 different bare metal electrodes. The metals that were more absorptive in the visible part of the spectrum tended to be poorer reflectors (see SI, Fig. S6), which reduced the overall active layer absorption (Fig. 3(a),(b)). Both Ag and Al had low absorption loss in the range of 350–600 nm (Ag absorbed between < 1 and 2% and Al absorbed between < 1 and 5%). Although Al became more absorptive at longer wavelengths, with absorption ranging from 5% to 18% between 600 and 800 nm, this did not significantly impact the amount of light absorbed by the active layer since P3HT does not

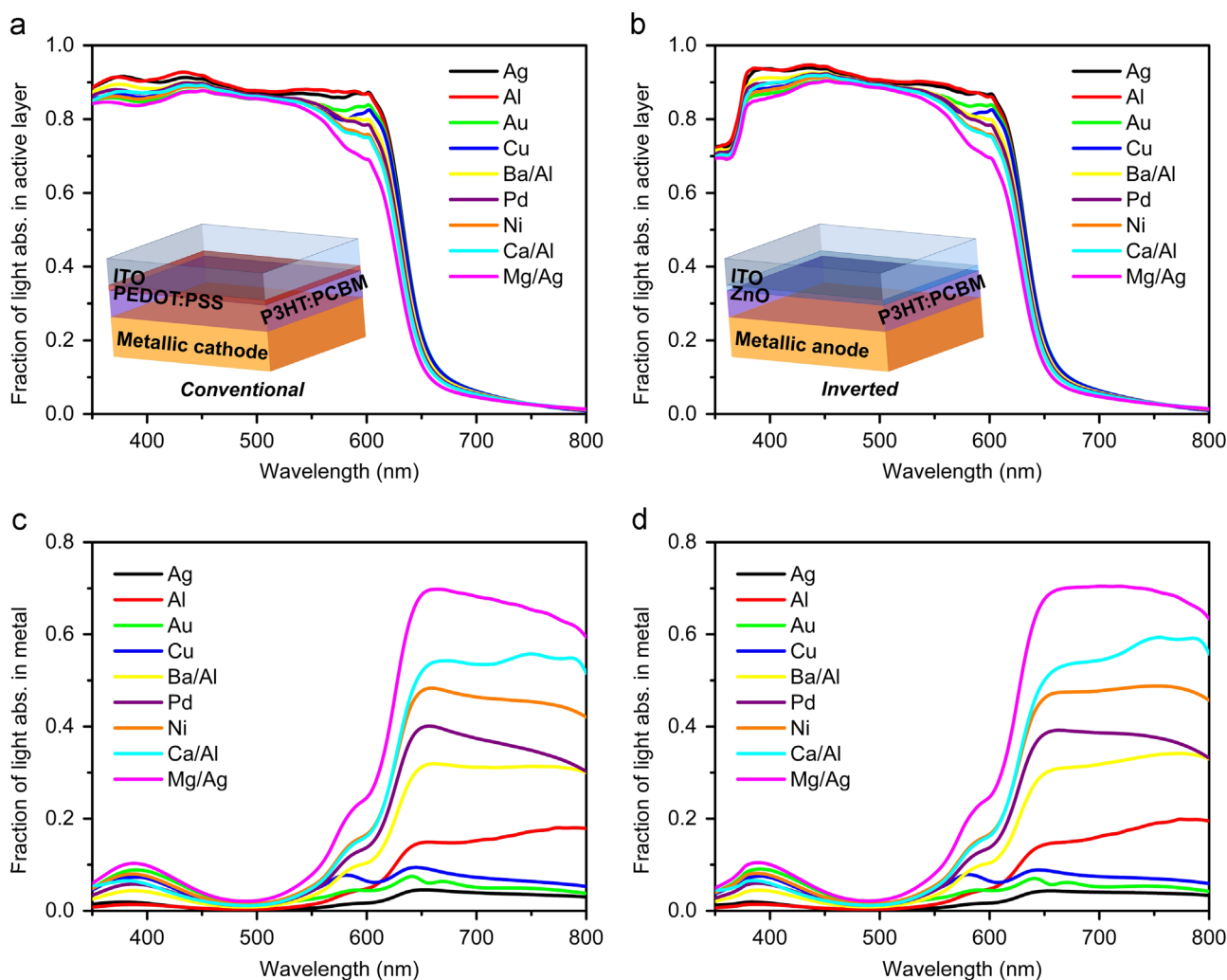


Fig. 3. Theoretical fractional absorption spectra (a),(b) in the active layer and (c),(d) in the metal for the conventional and inverted configurations for each bare metal cathode and anode studied, respectively. The fractional absorption spectra in the active layer and metal for the oxide- or fluoride-coated metals differed on average by < 10% across the visible spectrum (see SI, Fig. S4).

absorb strongly beyond 650 nm. For lower bandgap polymers (such as PCDTBT (a polycarbazole derivative) [77,123], PBDTT, or PTB7 (two benzodithiophene derivatives) [45,124]), longer wavelength absorption in Al electrodes may substantially reduce active layer absorption. Note that Ag absorbed less than 5% of light beyond 600 nm, making it more ideal for lower bandgap polymer absorbers. Copper and gold were both slightly more absorptive at shorter wavelengths, absorbing ~7% and 9%, respectively, at 390 nm, and, overall, absorbing up to 7% and 5% of light between 350 and 600 nm, respectively. This is attributed to interband absorption by Cu and Au in the range of 500–600 nm [125]. This region corresponded to the region of maximum absorption by P3HT:PCBM, which resulted in Au- or Cu- based electrodes reflecting less light (between 350 and 600 nm) back into the active layer compared with Ag- or Al- based electrodes. Although Cu and Au were less absorptive beyond 600 nm (5–7% for Cu and 6–10% for Au), P3HT does not absorb strongly beyond 650 nm, so the lower loss at longer wavelengths did not compensate the high loss at shorter wavelengths.

The remaining metals all followed a similar trend of absorbing less incident light in the region of 350–600 nm (where most of the light was absorbed by P3HT:PCBM) and absorbing much more beyond 600 nm. At 390 nm, the total light absorbed in the metal was 4.4%, 6.0%, 6.6%, 8%, and 10% for Ba/Al, Pd, Ca/Al, Ni, and Mg/Ag, respectively. Beyond 600 nm, the absorption of these metals

peaked near 650 nm, where the fraction of light absorbed by each metal was 31%, 40%, 48%, 53%, and 69% for Ba/Al, Pd, Ni, Ca/Al, and Mg/Ag, respectively. The low workfunction metals, Ba, Ca, and Mg, all tended to have high absorption losses, and would more than likely have exceeded the absorption losses in Pd and Ni if a comparable thickness was used for the low workfunction metals (200 nm). It should be noted that thicknesses reported in the literature for Ca range up to 50 nm [38]–80 nm [9], which would result in even greater parasitic absorption. Fractional absorption in the metal layer was similar for both conventional and inverted device configurations, except for a dip in metal layer absorption between ~350 and 380 nm, as described above. Less than 1% of the total (integrated) light was absorbed by each of the 2-nm-thick metal oxide/fluoride layers (see Fig. 2(e) and SI Table S2).

The fraction of light absorbed in the active layer, electrode layer (s) and front interlayers (defined here as ZnO/ITO and PEDOT:PSS/ITO for inverted and conventional devices, respectively) integrated over the 350–800 nm wavelength range is represented in Fig. 4 for both inverted and conventional devices along with calculated J_{sc} values. It was observed that the amount of light absorbed by the active layer increased with decreasing fraction of light absorbed by the metal (i.e., increasing reflectivity of the metal electrode; see SI Fig. S6) with the exception of NiO/Ni, Al and all metal oxide/fluoride-coated Al electrodes. Inverted devices tended to absorb more light in the active layer compared with conventional devices

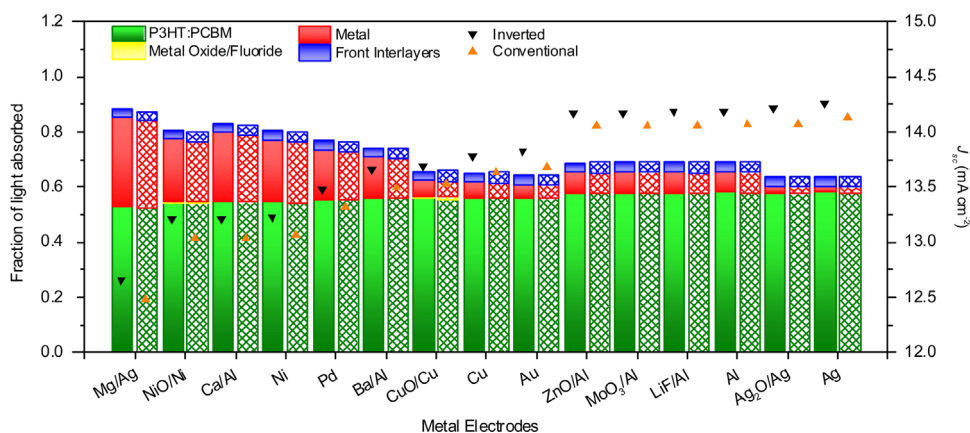


Fig. 4. Integrated absorption in the active layer, electrode layer(s), metal oxide/fluoride layers (where present) and front interlayers (defined here as ZnO/ITO and PEDOT:PSS/ITO for inverted and conventional devices, respectively) for devices with a range of different bare or coated metal electrodes. The left (solid) bar in each column corresponds to inverted devices and the right (hatched) bar to conventional devices. Overlaid are data points for the calculated J_{sc} values for each device (inverted black triangles for inverted devices, orange triangles for conventional devices). The layers and thicknesses used for the simulations are described in Section 2.1; the thicknesses of each layer were kept constant between conventional and inverted devices to minimize the optical interference effects due to changing layer thickness [51,52,99,102,121,122] (For interpretation of the references to color in this figure legend, the reader is referred to the web version of this article).

(see also SI Fig. S7). It was observed that the J_{sc} increased as the fraction of light absorbed in the active layer increased, but did not correlate with total absorbed light in the device (due to parasitic absorption in more absorptive metals such as Mg). In all cases, the J_{sc} of inverted devices was larger than that of conventional devices by 0.12–0.19 mA/cm², with inverted devices reaching a maximum J_{sc} of 14.26 mA/cm² for a Ag anode compared with 14.13 mA/cm² for a conventional device with a Ag cathode. This is attributed to the larger transmissivity of ZnO compared to PEDOT:PSS beyond 380 nm (see SI for details). Ag and Al electrodes, either bare or coated, resulted in the highest J_{sc} values in both conventional or inverted configurations; devices employing the low workfunction bilayer metal electrodes, Ni, and Pd resulted in the lowest J_{sc} values, with Mg/Ag having the lowest J_{sc} of 12.66 mA/cm² in the inverted configuration. Details of the simulation accuracy will be discussed in Section 4.5. The difference between 1 (i.e., total normalized incident light intensity) and the total integrated fraction of light absorbed in each device represents the fraction of light lost due to reflection; thus, if light trapping techniques, such as application of anti-reflection coatings, are employed, then BHJ-OPVs with the lowest total absorption (i.e., Ag, Au, Cu metal electrodes) have the most potential for improvement.

4.4. Power conversion efficiency

Fig. 5 shows the theoretical power conversion efficiency for all of the device and electrode types. It is apparent that low workfunction metals (bare or coated) (e.g., LiF/Al, Ba/Al, Ca/Al, Mg/Al) are necessary for high-efficiency conventional devices (efficiencies of up to 6.77% for LiF/Al); however, lower workfunction metals are typically not stable in air and are very likely to have relatively short operational lifetimes [5,121]. Higher workfunction metal electrodes (e.g., Au, Pd, Ni), native metal oxide-coated metal electrodes (e.g., Ag₂O/Ag, CuO/Cu, NiO/Ni), or high workfunction *p*-type metal oxide-coated metal electrodes (e.g., MoO₃/Al) are necessary for high-efficiency inverted devices (efficiency of up to 6.70% for Ag₂O/Ag) and are expected to be more stable in ambient conditions [5,121]. It is notable that *p*-type native metal oxide formation, which is likely to occur for Ag, Cu, and Ni when exposed to air [1,2,6–8] or if oxygen permeates through the device [1,4,5], can result in high-efficiency inverted devices, but is detrimental to conventional device performance; therefore the performance of conventional devices is likely to degrade with

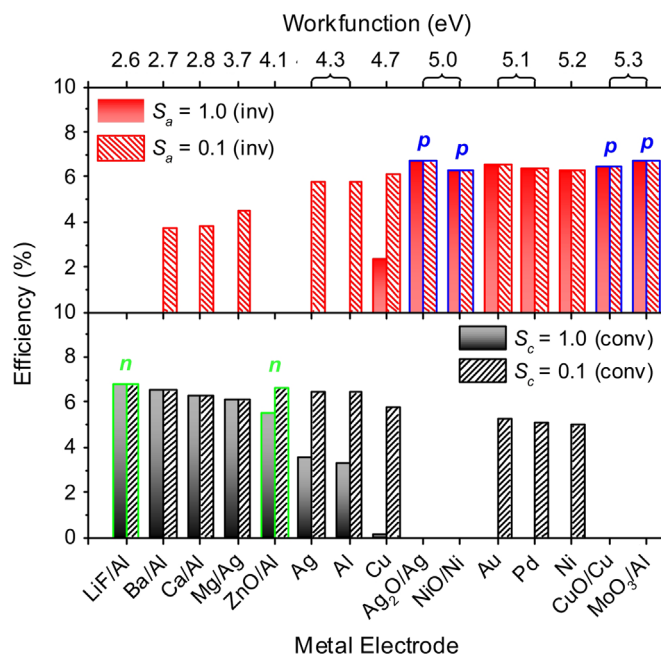


Fig. 5. Calculated power conversion efficiency for the 9 bare metal and 6 coated metal electrodes studied for inverted (top) and conventional (bottom) configurations calculated using the data in Fig. 2, and the J_{sc} values shown in Fig. 3(e). The blue outlined bars refer to *p*-type metal oxide-coated metals and the green outlined bars refer to the *n*-type metal oxide- or fluoride-coated metals (For interpretation of the references to color in this figure legend, the reader is referred to the web version of this article).

aging or oxidation of the electrode [5,46,121]. Based on our computations, we believe that inverted BHJ-OPVs can theoretically perform as well as or better than conventional BHJ-OPVs, and one possible limitation is the higher R_s for inverted devices. However, it could be possible to develop methods of reducing the R_s of inverted devices (e.g., use of more conductive ETLs, doping ZnO to improve conductivity, etc.).

4.5. Simulation accuracy

The accuracy of the numerical results presented here was validated through a comparison with experimental data from

several different metal electrode-dependent studies. All tabulated literature values can be found in the SI. Eo et al. studied conventional BHJ-OPVs based on P3HT:PCBM with varying metal cathode from LiF/Al, Ca/Al, Mg/Al, Al, and Au and found that the J_{sc} was lowest for Ca and Mg based devices (8.21 and 9.17 mA/cm², respectively) and increased for less lossy electrodes (LiF/Al, Al, and Au had values of 9.74, 9.27, and 8.28 mA/cm²) [39]. Apart from LiF, they observed similar trends in the J_{sc} data as reported here (e.g., $J_{sc}^{Al} > J_{sc}^{Au} > J_{sc}^{Ca}$ and J_{sc}^{Mg}). Mg had a higher J_{sc} than Ca, but both were supported by Al (whereas in this study, we chose to support Mg by Ag [40]). All of the J_{sc} values from that study are lower by ~ 5 mA/cm² compared to the values reported here (i.e., 60–70% of our calculated values), which we attribute to $\eta_{IQE} < 100\%$ due to recombination (typical η_{IQE} values range from $\sim 50\%$ to 80% between 350 and 650 nm), exciton decay losses and differences device layer geometry. However, as we report in the SI, since the generation rate profiles (Fig. S3) were similar for each metal electrode, and the active layer thickness and material were kept constant, we expect our J_{sc} to be an overestimate of the experimental J_{sc} values and represent the maximum possible J_{sc} . The trends in J_{sc} with varying electrode and device type should still hold when a non-ideal η_{IQE} is considered. Another possible factor that could result in a lowering of empirical J_{sc} values relative to those calculated here is the higher series resistance expected for bare Al electrodes [126]. This is presumably the reason why the LiF/Al electrode outperforms the Al electrode in the study by Eo et al., as LiF could potentially protect the active layer from reactions with Al, possibly reducing the series resistance [39].

The $V_{oc,max}$ reported here (0.7 V) is also considered an upper limit for the P3HT:PCBM blend [127]. In experiment, the V_{oc} for P3HT:PCBM BHJ-OPVs is typically around 0.5–0.6 max [32–35,37], although it has been reported as high as 0.67 [2]. The FF_0 values reported here are certainly higher (~ 0.76) than most experimental values for FF (typically in the range of 0.5–0.67 [15,32–34,37]), however when parasitic resistances were considered, values closer to the experimental values were calculated (~ 0.69). Due to the high J_{sc} values reported here, the total η_p values are slightly higher ($\sim 6.7\%$) than what is frequently observed experimentally ($\sim 5\%$) [32–35,37]. However, the purpose of these calculations is to compare and obtain insight into the trends in conventional and inverted device performance with electrode type, rather than directly predicting empirical performance parameters (particularly since there is uncertainty in the precise values of the energy levels, η_{IQE} , n_d , R_s , R_{sh} , and the optical constants, and slight changes in any of these values can result in large changes in J_{sc} , V_{oc} and FF).

5. Conclusions

In summary, we have calculated the electronic and optical performance parameters for various metal electrodes, with and without metal oxide/fluoride coatings for inverted and conventional bulk-heterojunction organic photovoltaic (BHJ-OPV) device configurations. We have quantified the open-circuit voltage and fill factor of inverted and conventional BHJ-OPVs for 2 extreme cases of (1) strong interface dipole between the organic active layer and the metal and (2) no interface dipole between the organic active layer and metal or metal oxide/fluoride. We have also quantitatively shown that inverted BHJ-OPVs can outperform conventional BHJ-OPVs in terms of their short-circuit current density values due to differences in the optical properties of the hole and electron transport layers for conventional and inverted devices, respectively and that addition of an ultrathin metal oxide/fluoride interfacial layer does not greatly affect these values based on optical simulations. Based on our efficiency calculations, we

have shown that (1) high workfunction metals are necessary for high-efficiency inverted device performance, and (2) native metal oxide formation on metal electrodes can result in high-efficiency inverted devices but can also degrade conventional device efficiency. We recommend that future BHJ-OPV research should focus on the inverted configuration, which is known to be more air-stable than its conventional counterpart, and can theoretically perform as well as, or superior to, conventional devices.

Acknowledgments

The authors gratefully acknowledge support by National Science Foundation Grant no. 0903661 “Nanotechnology for Clean Energy IGERT,” in part by National Science Foundation (DMR_1309459), a Corning Inc. fellowship, Rutgers’ Institute for Adv. Mater Devices and Nanotechnology, and Rutgers’ Aresty undergraduate research fellowship program. The authors thank Coleen Nemes, Gary Cheung, Binxing Yu, and Jesse Kohl for useful discussion.

Appendix A. Supplementary material

Supplementary data associated with this article can be found in the online version at <http://dx.doi.org/10.1016/j.solmat.2013.09.041>.

References

- [1] M.T. Lloyd, D.C. Olson, P. Lu, E. Fang, D.L. Moore, M.S. White, et al., Impact of contact evolution on the shelf life of organic solar cells, *J. Mater. Chem.* 19 (2009) 7638–7780.
- [2] S.K. Hau, H.-L. Yip, N.S. Baek, J. Zou, K. O'Malley, A.K.-Y. Jen, Air-stable inverted flexible polymer solar cells using zinc oxide nanoparticles as an electron selective layer, *Appl. Phys. Lett.* 92 (2008) 253301.
- [3] S.R. Ferreira, P. Lu, Y.-J. Lee, R.J. Davis, J.W.P. Hsu, Effect of zinc oxide electron transport layers on performance and shelf life of organic bulk heterojunction devices, *J. Phys. Chem. C* 115 (2011) 13471–13475.
- [4] M. Jørgensen, K. Norrman, F.C. Krebs, Stability/degradation of polymer solar cells, *Sol. Energy Mater. Sol. Cells* 92 (2008) 686–714.
- [5] M. Jørgensen, K. Norrman, S.A. Gevorgyan, T. Tromholt, B. Andreasen, F.C. Krebs, Stability of polymer solar cells, *Adv. Mater.* 24 (2012) 580–612.
- [6] H. Won Choi, S. Young Kim, K.-B. Kim, Y.-H. Tak, J.-L. Lee, Enhancement of hole injection using O₂ plasma-treated Ag anode for top-emitting organic light-emitting diodes, *Appl. Phys. Lett.* 86 (2005) 012104-1–012104-3.
- [7] J.B. Kim, C.S. Kim, Y.S. Kim and Y.-L. Loo, Oxidation of silver electrodes induces transition from conventional to inverted photovoltaic characteristics in polymer solar cells, *Appl. Phys. Lett.* 95, 2009, 183301-1–183301-3.
- [8] S. Kim, K. Hong, K. Kim, I. Lee, J.-L. Lee, Phase-controllable copper oxides for an efficient anode interfacial layer in organic light-emitting diodes, *J. Mater. Chem.* 22 (2012) 2039–2044.
- [9] C.J. Brabec, A. Cravino, D. Meissner, N.S. Sariciftci, T. Fromherz, M.T. Rispens, et al., Origin of the open circuit voltage of plastic solar cells, *Adv. Funct. Mater.* 11 (2001) 374–380.
- [10] W. Cai, X. Gong, Y. Cao, Polymer solar cells: Recent development and possible routes for improvement in the performance, *Sol. Energy Mater. Sol. Cells* 94 (2010) 114–127.
- [11] A. Moliton, J.-M. Nunzi, How to model the behaviour of organic photovoltaic cells, *Polym. Int.* 55 (2006) 583–600.
- [12] M.C. Scharber, D. Mühlbacher, M. Koppe, P. Denk, C. Waldauf, A.J. Heeger, et al., Design rules for donors in bulk-heterojunction solar cells – towards 10% energy-conversion efficiency, *Adv. Mater.* 18 (2006) 789–794.
- [13] P. Heremans, D. Cheyns, B.P. Rand, Strategies for increasing the efficiency of heterojunction organic solar cells: material selection and device architecture, *Acc. Chem. Res.* 42 (2009) 1740–1747.
- [14] M. Glatthaar, M. Niggemann, B. Zimmermann, P. Lewer, M. Riede, A. Hinsch, et al., Organic solar cells using inverted layer sequence, *Thin Solid Films* 491 (2005) 298–300.
- [15] F. Zhang, X. Xu, W. Tang, J. Zhang, Z. Zhuo, J. Wang, et al., Recent development of the inverted configuration organic solar cells, *Sol. Energy Mater. Sol. Cells* 95 (2011) 1785–1799.
- [16] S.K. Hau, K.M. O'Malley, Y. Cheng, H. Yip, H. Ma, A.K. Jen, Optimization of active layer and anode electrode for high-performance inverted bulk-heterojunction solar cells, *IEEE J. Quantum Electron.* 16 (2010) 1665–1675.
- [17] M.S. White, D.C. Olson, S.E. Shaheen, N. Kopidakis, D.S. Ginley, Inverted bulk-heterojunction organic photovoltaic device using a solution-derived ZnO underlayer, *Appl. Phys. Lett.* 89 (2006) 143517-1–143517-3.

- [18] R. Steim, S.A. Choulis, P. Schilinsky, C.J. Brabec, Interface modification for highly efficient organic photovoltaics, *Appl. Phys. Lett.* 92 (2008) 093303–1–093303-3.
- [19] H.-H. Liao, L.-M. Chen, Z. Xu, G. Li, Y. Yang, Highly efficient inverted polymer solar cell by low temperature annealing of Cs_2CO_3 interlayer, *Appl. Phys. Lett.* 92 (2008) 173303–1–173303-3.
- [20] C. Waldauf, M. Morana, P. Denk, P. Schilinsky, K. Coakley, S.A. Choulis, et al., Highly efficient inverted organic photovoltaics using solution based titanium oxide as electron selective contact, *Appl. Phys. Lett.* 89 (2006) 233517–1–233517-3.
- [21] C.-Y. Li, T.-C. Wen, T.-H. Lee, T.-F. Guo, J.-C.-A. Huang, Y.-C. Lin, et al., An inverted polymer photovoltaic cell with increased air stability obtained by employing novel hole/electron collecting layers, *J. Mater. Chem.* 19 (2009) 1643–1647.
- [22] S.A. Carter, M. Angelopoulos, S. Karg, P.J. Brock, J.C. Scott, Polymeric anodes for improved polymer light-emitting diode performance, *Appl. Phys. Lett.* 70 (1997) 2067–2069.
- [23] J.C. Scott, S.A. Carter, S. Karg, M. Angelopoulos, Polymeric anodes for organic light-emitting diodes, *Synth. Met.* 85 (1997) 1197–1200.
- [24] G. Greczynski, T. Kugler, M. Keil, W. Osikowicz, M. Fahlman, W. Salaneck, Photoelectron spectroscopy of thin films of PEDOT–PSS conjugated polymer blend: a mini-review and some new results, *J. Electron. Spectrosc. Relat. Phenom.* 121 (2001) 1–17.
- [25] M.P. de Jong, L.J. van IJendoorn, M.J.A. de Voigt, Stability of the interface between indium-tin-oxide and poly(3,4-ethylenedioxythiophene):poly(styrenesulfonate) in polymer light-emitting diodes, *Appl. Phys. Lett.* 77 (2000) 2255–2257.
- [26] J.-S. Huang, C.-Y. Chou, M.-Y. Liu, K.-H. Tsai, W.-H. Lin, C.-F. Lin, Solution-processed vanadium oxide as an anode interlayer for inverted polymer solar cells hybridized with ZnO nanorods, *Org. Electron.* 10 (2009) 1060–1065.
- [27] K. Takanezawa, K. Tajima, K. Hashimoto, Efficiency enhancement of polymer photovoltaic devices hybridized with ZnO nanorod arrays by the introduction of a vanadium oxide buffer layer, *Appl. Phys. Lett.* 93 (2008) 063308–1–063308-3.
- [28] C. Tao, S. Ruan, G. Xie, X. Kong, L. Shen, F. Meng, et al., Role of tungsten oxide in inverted polymer solar cells, *Appl. Phys. Lett.* 94 (2009) 043311–1–043311-3.
- [29] D.W. Zhao, P. Liu, X.W. Sun, S.T. Tan, L. Ke, A.K.K. Kyaw, An inverted organic solar cell with an ultrathin Ca electron-transporting layer and MoO_3 hole-transporting layer, *Appl. Phys. Lett.* 95 (2009) 153304–1–153304-3.
- [30] A.K.K. Kyaw, X.W. Sun, C.Y. Jiang, G.Q. Lo, D.W. Zhao, D.L. Kwong, An inverted organic solar cell employing a sol-gel derived ZnO electron selective layer and thermal evaporated MoO_3 hole selective layer, *Appl. Phys. Lett.* 93 (2008) 221107–1–221107-3.
- [31] J. Ajuria, I. Etxebarria, W. Cambarau, U. Muñecas, R. Tena-Zaera, J.C. Jimeno, et al., Inverted ITO-free organic solar cells based on p and n semiconducting oxides. New designs for integration in tandem cells, top or bottom detecting devices, and photovoltaic windows, *Energy Environ. Sci.* 4 (2011) 453–458.
- [32] W. Ma, C. Yang, X. Gong, K. Lee, A.J. Heeger, Thermally stable, efficient polymer solar cells with nanoscale control of the interpenetrating network morphology, *Adv. Funct. Mater.* 15 (2005) 1617–1622.
- [33] G. Li, V. Shrotriya, Y. Yao, Y. Yang, Investigation of annealing effects and film thickness dependence of polymer solar cells based on poly(3-hexylthiophene), *J. Appl. Phys.* 98 (2005) 043704–1–043704-5.
- [34] G. Li, V. Shrotriya, J. Huang, Y. Yao, T. Moriarty, K. Emery, et al., High-efficiency solution processable polymer photovoltaic cells by self-organization of polymer blends, *Nat. Mater.* 4 (2005) 864–868.
- [35] Y. Kim, S. Cook, S.M. Tuladhar, S.A. Choulis, J. Nelson, J.R. Durrant, et al., A strong regioregularity effect in self-organizing conjugated polymer films and high-efficiency polythiophene:fullerene solar cells, *Nat. Mater.* 5 (2006) 197–203.
- [36] M.D. Irwin, D.B. Buchholz, A.W. Hains, R.P.H. Chang, T.J. Marks, p-Type semiconducting nickel oxide as an efficiency-enhancing anode interfacial layer in polymer bulk-heterojunction solar cells, *PNAS* 105 (2008) 2783–2787.
- [37] G. Dennler, M.C. Scharber, C.J. Brabec, Polymer-fullerene bulk-heterojunction solar cells, *Adv. Mater.* 21 (2009) 1323–1338.
- [38] A. Hadipour, D. Cheyns, P. Heremans, B.P. Rand, Electrode considerations for the optical enhancement of organic bulk heterojunction solar cells, *Adv. Energy Mater.* 1 (2011) 930–935.
- [39] Y.S. Eo, H.W. Rhee, B.D. Chin, J.-W. Yu, Influence of metal cathode for organic photovoltaic device performance, *Synth. Met.* 159 (2009) 1910–1913.
- [40] M.O. Reese, M.S. White, G. Rumbles, D.S. Ginley, S.E. Shaheen, Optimal negative electrodes for poly(3-hexylthiophene): [6,6]-phenyl C_{61} -butyric acid methyl ester bulk heterojunction photovoltaic devices, *Appl. Phys. Lett.* 92 (2008) 053307–1–053307-3.
- [41] V.D. Mihailetschi, P.W.M. Blom, J.C. Hummelen, M.T. Rispen, Cathode dependence of the open-circuit voltage of polymer:fullerene bulk heterojunction solar cells, *J. Appl. Phys.* 94 (2003) 6849–6854.
- [42] M.F. Lo, T.W. Ng, T.Z. Liu, V.A.L. Roy, S.L. Lai, M.K. Fung, et al., Limits of open circuit voltage in organic photovoltaic devices, *Appl. Phys. Lett.* 96 (2010) 113303.
- [43] S. Albrecht, S. Schäfer, I. Lange, S. Yilmaz, I. Dumsch, S. Allard, et al., Light management in PCPDTBT-PC₇₀BM solar cells: A comparison of standard and inverted device structures, *Org. Electron.* 13 (2012) 615–622.
- [44] J. Zou, H.-L. Yip, Y. Zhang, Y. Gao, S.-C. Chien, K. O'Malley, et al., High-performance inverted polymer solar cells: device characterization, optical modeling, and hole-transporting modifications, *Adv. Funct. Mater.* 22 (2012) 2804–2811.
- [45] Z. He, C. Zhong, S. Su, M. Xu, H. Wu, Y. Cao, Enhanced power-conversion efficiency in polymer solar cells using an inverted device structure, *Nat. Photonics* 6 (2012) 591–595.
- [46] S. Schumann, R. Da Campo, B. Illy, A.C. Cruickshank, M.A. McLachlan, M.P. Ryan, et al., Inverted organic photovoltaic devices with high efficiency and stability based on metal oxide charge extraction layers, *J. Mater. Chem.* 21 (2011) 2381–2386.
- [47] L.J.A. Koster, V.D. Mihailetschi, P.W.M. Blom, Ultimate efficiency of polymer/fullerene bulk heterojunction solar cells, *Appl. Phys. Lett.* 88 (2006) 093511–1–093511-3.
- [48] P.W.M. Blom, V.D. Mihailetschi, L.J.A. Koster, D.E. Markov, Device physics of polymer: fullerene bulk heterojunction solar cells, *Adv. Mater.* 19 (2007) 1551–1566.
- [49] J.D. Servaites, M.A. Ratner, T.J. Marks, Practical efficiency limits in organic photovoltaic cells: functional dependence of fill factor and external quantum efficiency, *Appl. Phys. Lett.* 95 (2009) 163302–1–163302-3.
- [50] H. Hoppe, N. Arnold, N.S. Sariciftci, D. Meissner, Modeling the optical absorption within conjugated polymer/fullerene-based bulk-heterojunction organic solar cells, *Sol. Energy Mater. Sol. Cells* 80 (2003) 105–113.
- [51] F. Monestier, J.-J. Simon, P. Torchio, L. Escoubas, F. Flory, S. Bailly, et al., Modeling the short-circuit current density of polymer solar cells based on P3HT:PCBM blend, *Sol. Energy Mater. Sol. Cells* 91 (2007) 405–410.
- [52] G.F. Burkhard, E.T. Hoke, M.D. McGehee, Accounting for interference, scattering, and electrode absorption to make accurate internal quantum efficiency measurements in organic and other thin solar cells, *Adv. Mater.* 22 (2010) 3293–3297.
- [53] Y. Min Nam, J. Huh, W. Ho Jo, Optimization of thickness and morphology of active layer for high performance of bulk-heterojunction organic solar cells, *Sol. Energy Mater. Sol. Cells* 94 (2010) 1118–1124.
- [54] R. Betancur, A. Martínez-Otero, X. Elias, P. Romero-Gómez, S. Colodrero, H. Miguez, et al., Optical interference for the matching of the external and internal quantum efficiencies in organic photovoltaic cells, *Sol. Energy Mater. Sol. Cells* 104 (2012) 87–91.
- [55] M.Y. Song, K.-J. Kim, D.Y. Kim, Enhancement of photovoltaic characteristics using a PEDOT interlayer in $\text{TiO}_2/\text{MEH-PPV}$ heterojunction devices, *Sol. Energy Mater. Sol. Cells* 85 (2004) 31–39.
- [56] Y. Şahin, S. Alem, R. de Bettignies, J.-M. Nunzi, Development of air stable polymer solar cells using an inverted gold on top anode structure, *Thin Solid Films* 476 (2005) 340–343.
- [57] A. Watanabe, A. Kasuya, Effect of atmospheres on the open-circuit photovoltage of nanoporous $\text{TiO}_2/\text{poly}(3\text{-hexylthiophene})$ heterojunction solar cell, *Thin Solid Films* 483 (2005) 358–366.
- [58] S. Braun, W.R. Salaneck, M. Fahlman, Energy-level alignment at organic/metal and organic/organic interfaces, *Adv. Mater.* 21 (2009) 1450–1472.
- [59] I.G. Hill, A. Rajagopal, A. Kahn, Y. Hu, Molecular level alignment at organic semiconductor-metal interfaces, *Appl. Phys. Lett.* 73 (1998) 662–664.
- [60] S.E. Shaheen, G.E. Jabbour, M.M. Morrell, Y. Kawabe, B. Kippelen, N. Peyghambarian, et al., Bright blue organic light-emitting diode with improved color purity using a LiF/Al cathode, *J. Appl. Phys.* 84 (1998) 2324–2327.
- [61] H.B. Michaelson, The work function of the elements and its periodicity, *J. Appl. Phys.* 48 (1977) 4729–4733.
- [62] J. Olivier, B. Servet, M. Vergnolle, M. Mosca, G. Garry, Stability / instability of conductivity and work function changes of ITO thin films, UV-irradiated in air or vacuum. Measurements by the four-probe method and by Kelvin force microscopy, *Synth. Met.* 122 (2001) 87–89.
- [63] U. Kumar Barik, S. Srinivasan, C. Nagendra, A. Subrahmanyam, Electrical and optical properties of reactive DC magnetron sputtered silver oxide thin films: role of oxygen, *Thin Solid Films* 429 (2003) 129–134.
- [64] K. Hong, J.-L. Lee, Inverted top-emitting organic light-emitting diodes using transparent silver oxide anode formed by oxygen plasma, *Electrochem. Solid-State Lett.* 11 (2008) H29.
- [65] M. Zhang, T.-L. Chiu, C.-F. Lin, J.-H. Lee, J.-K. Wang, Y. Wu, Roughness characterization of silver oxide anodes for use in efficient top-illuminated organic solar cells, *Sol. Energy Mater. Sol. Cells* 95 (2011) 2606–2609.
- [66] F.P. Koffyberg, F.A. Benko, A photoelectrochemical determination of the position of the conduction and valence band edges of p-type CuO, *J. Appl. Phys.* 53 (1982) 1173–1177.
- [67] G. Mangamma, V. Jayaraman, T. Gnanasekaran, G. Periaswami, Effects of silica additions on H_2S sensing properties of CuO-SnO_2 sensors, *Sens. Actuators* B. 53 (1998) 133–139.
- [68] V. Shrotriya, G. Li, Y. Yao, C.-W. Chu, Y. Yang, Transition metal oxides as the buffer layer for polymer photovoltaic cells, *Appl. Phys. Lett.* 88 (2006) 073508–1–073508-3.
- [69] T. Yang, M. Wang, C. Duan, X. Hu, L. Huang, J. Peng, et al., Inverted polymer solar cells with 8.4% efficiency by conjugated polyelectrolyte, *Energy Environ. Sci.* 5 (2012) 8208–8214.
- [70] J. Cao, X. Jiang, Z. Zhang, MoO_3 modified Ag anode for top-emitting organic light-emitting devices, *Appl. Phys. Lett.* 89 (2006) 252108.
- [71] X. Gong, Toward high performance inverted polymer solar cells, *Polymer* 53 (2012) 5437–5448.
- [72] S.S. Jeong, A. Mittiga, E. Salza, A. Masci, S. Passerini, Electrodeposited $\text{ZnO}/\text{Cu}_2\text{O}$ heterojunction solar cells, *Electrochim. Acta* 53 (2008) 2226–2231.
- [73] X. Bulliard, S.-G. Ihn, S. Yun, Y. Kim, D. Choi, J.-Y. Choi, et al., Enhanced performance in polymer solar cells by surface energy control, *Adv. Funct. Mater.* 20 (2010) 4381–4387.

- [74] L.-M. Chen, Z. Hong, G. Li, Y. Yang, Recent progress in polymer solar cells: manipulation of polymer:fullerene morphology and the formation of efficient inverted polymer solar cells, *Adv. Mater.* 21 (2009) 1434–1449.
- [75] J.H. Lee, J.-H. Shin, J.Y. Song, W. Wang, R. Schlaf, K.J. Kim, et al., Interface formation between ZnO nanorod arrays and polymers (PCBM and P3HT) for organic solar cells, *J. Phys. Chem. C* 116 (2012) 26342–26348.
- [76] H.O. Seo, S. Park, W.H. Shim, K. Kim, K.H. Lee, M.Y. Jo, et al., Ultrathin TiO₂ films on ZnO electron-collecting layers of inverted organic solar cell, *J. Phys. Chem. C* 115 (2011) 21517–21520.
- [77] S.H. Park, A. Roy, S. Beaupr , S. Cho, N. Coates, J.S. Moon, et al., Bulk heterojunction solar cells with internal quantum efficiency approaching 100%, *Nat. Photonics* 3 (2009) 297–302.
- [78] C. Waldauf, P. Schilinsky, J. Hauch, C.J. Brabec, Material and device concepts for organic photovoltaics: towards competitive efficiencies, *Thin Solid Films* 451–452 (2004) 503–507.
- [79] N. Li, T. Stubhan, N.A. Luechinger, S.C. Halim, G.J. Matt, T. Ameri, et al., Inverted structure organic photovoltaic devices employing a low temperature solution processed WO₃ anode buffer layer, *Org. Electron.* 13 (2012) 2479–2484.
- [80] G. Li, C.-W. Chu, V. Shrotriya, J. Huang, Y. Yang, Efficient inverted polymer solar cells, *Appl. Phys. Lett.* 88 (2006) 253503-1–253503-3.
- [81] S. Wilkens, D. Scheunemann, V. Wilkens, J. Parisi, H. Borchert, Improvement of ITO-free inverted polymer-based solar cells by using colloidal zinc oxide nanocrystals as electron-selective buffer layer, *Org. Electron.* 13 (2012) 2386–2394.
- [82] H. Zhou, L. Yang, S. Stoneking, W. You, A weak donor–strong acceptor strategy to design ideal polymers for organic solar cells, *ACS Appl. Mater. Interfaces* 2 (2010) 1377–1383.
- [83] C. Genet, T.W. Ebbesen, Light in tiny holes, *Nature* 445 (2007) 39–46.
- [84] W. Hu, K. Manabe, T. Furukawa, M. Matsumura, Lowering of operational voltage of organic electroluminescent devices by coating indium–tin–oxide electrodes with a thin CuO_x layer, *Appl. Phys. Lett.* 80 (2002) 2640.
- [85] S.E. Shaheen, C.J. Brabec, N.S. Sariciftci, F. Padinger, T. Fromherz, J.C. Hummelen, 2.5% Efficient organic plastic solar cells, *Appl. Phys. Lett.* 78 (2001) 841–843.
- [86] C.J. Brabec, S.E. Shaheen, C. Winder, N.S. Sariciftci, P. Denk, Effect of LiF/metal electrodes on the performance of plastic solar cells, *Appl. Phys. Lett.* 80 (2002) 1288–1290.
- [87] X. Buwen, S. Yafeng, M. Meng, L. Chuannan, Enhancement of hole injection with an ultra-thin Ag₂O modified anode in organic light-emitting diodes, *Microelectron. J.* 36 (2005) 105–108.
- [88] S. Kim, K. Hong, K. Kim, I. Lee, K.-B. Kim, D.Y. Lee, et al., Hole Injection Layer of Thermally evaporated copper oxide for top emitting organic light emitting diodes, *J. Electrochem. Soc.* 157 (2010) J347–J350.
- [89] I.-M. Chan, T.-Y. Hsu, F.C. Hong, Enhanced hole injections in organic light-emitting devices by depositing nickel oxide on indium tin oxide anode, *Appl. Phys. Lett.* 81 (2002) 1899–1901.
- [90] I.-M. Chan, F.C. Hong, Improved performance of the single-layer and double-layer organic light emitting diodes by nickel oxide coated indium tin oxide anode, *Thin Solid Films* 450 (2004) 304–311.
- [91] C.-W. Chen, P.-Y. Hsieh, H.-H. Chiang, C.-L. Lin, H.-M. Wu and C.-C. Wu, Top-emitting organic light-emitting devices using surface-modified Ag anode, *Appl. Phys. Lett.* 83, 2003, 5127–5129.
- [92] M.-Y. Lin, C.-Y. Lee, S.-C. Shiu, I.-J. Wang, J.-Y. Sun, W.-H. Wu, et al., Sol–gel processed CuO_x thin film as an anode interlayer for inverted polymer solar cells, *Org. Electron.* 11 (2010) 1828–1834.
- [93] M. Wang, F. Xie, W. Xie, S. Zheng, N. Ke, J. Chen, et al., Device lifetime improvement of polymer-based bulk heterojunction solar cells by incorporating copper oxide layer at Al cathode, *Appl. Phys. Lett.* 98 (2011) 183304-1–183304-3.
- [94] F.C. Krebs, All solution roll-to-roll processed polymer solar cells free from indium–tin–oxide and vacuum coating steps, *Organic Electronics* 10 (2009) 761–768.
- [95] D. Angmo, M. H sel, F.C. Krebs, All solution processing of ITO-free organic solar cell modules directly on barrier foil, *Sol. Energy Mater. Sol. Cells* 107 (2012) 329–336.
- [96] B. Rand, D. Burk, S. Forrest, Offset energies at organic semiconductor heterojunctions and their influence on the open-circuit voltage of thin-film solar cells, *Phys. Rev. B* 75 (2007) 115327-1–115327-3.
- [97] H. Ishii, K. Sugiyama, E. Ito, K. Seki, Energy level alignment and interfacial electronic structures at organic/metal and organic/organic interfaces, *Adv. Mater.* 11 (1999) 605–625.
- [98] Z. Xu, L.-M. Chen, M.-H. Chen, G. Li, Y. Yang, Energy level alignment of poly(3-hexylthiophene): [6,6]-phenyl C₆₁ butyric acid methyl ester bulk heterojunction, *Appl. Phys. Lett.* 95 (2009) 013301-1–013301-3.
- [99] C. Tengstedt, W. Osikowicz, W.R. Salaneck, I.D. Parker, C.-H. Hsu, M. Fahlman, Fermi-level pinning at conjugated polymer interfaces, *Appl. Phys. Lett.* 88 (2006) 053502-1–053502-3.
- [100] M.A. Green, Accuracy of analytical expressions for solar cell fill factors, *Solar Cells* 7 (1982) 337–340.
- [101] P. Peumans, A. Yakimov, S.R. Forrest, Small molecular weight organic thin-film photodetectors and solar cells, *J. Appl. Phys.* 93 (2003) 3693–3723.
- [102] L.A.A. Pettersson, L.S. Roman, O. Ingan s, Modeling photocurrent action spectra of photovoltaic devices based on organic thin films, *J. Appl. Phys.* 86 (1999) 487–496.
- [103] Lumerical FDTD Solutions, version 7.5.7; Lumerical Solutions, Inc.: Vancouver, BC, 2011.
- [104] X. He, F. Gao, G. Tu, D.G. Hasko, S. H ttner, N.C. Greenham, et al., Formation of well-ordered heterojunctions in polymer:PCBM photovoltaic devices, *Adv. Funct. Mater.* 21 (2011) 139–146.
- [105] M.-S. Kim, J.-S. Kim, J.C. Cho, M. Shtein, L.J. Guo, J. Kim, Flexible conjugated polymer photovoltaic cells with controlled heterojunctions fabricated using nanoimprint lithography, *Appl. Phys. Lett.* 90 (2007) 123113-1–123113-3.
- [106] H. Xin, G. Ren, F.S. Kim, S.A. Jenekhe, Bulk heterojunction solar cells from poly(3-butylthiophene)/fullerene blends: in situ self-assembly of nanowires, morphology, charge transport, and photovoltaic properties, *Chem. Mater.* 20 (2008) 6199–6207.
- [107] X. Yang, J. Loos, S.C. Veenstra, W.J.H. Verhees, M.M. Wienk, J.M. Kroon, et al., Nanoscale morphology of high-performance polymer solar cells, *Nano Lett.* 5 (2005) 579–583.
- [108] G.K. Mor, K. Shankar, M. Paulose, O.K. Varghese, C.A. Grimes, High efficiency double heterojunction polymer photovoltaic cells using highly ordered TiO₂ nanotube arrays, *Appl. Phys. Lett.* 91 (2007) 152111-1–152111-3.
- [109] B.P. Rand, P. Peumans, S.R. Forrest, Long-range absorption enhancement in organic tandem thin-film solar cells containing silver nanoclusters, *J. Appl. Phys.* 96 (2004) 7519–7526.
- [110] Q. Gan, F.J. Bartoli, Z.H. Kafafi, Plasmonic-enhanced organic photovoltaics: breaking the 10% efficiency barrier, *Adv. Mater.* 25 (2013) 2385–2396.
- [111] B. Zeng, Q. Gan, Z.H. Kafafi, F.J. Bartoli, Polymeric photovoltaics with various metallic plasmonic nanostructures, *J. Appl. Phys.* 113 (2013) 063109-1–063109-10.
- [112] S.Y. Chou, W. Ding, Ultrathin, high efficiency, broad-band, omni-acceptance, organic solar cells enhanced by plasmonic cavity with subwavelength hole array, *Opt. Express* 21 (2013) A60–A76.
- [113] M. Polyanskiy, Refractive Index Database. (<http://refractiveindex.info>) (accessed Feb 2012).
- [114] K. Postava, H. Sueki, M. Aoyama, T. Yamaguchi, C. Ino, Y. Igasaki, et al., Spectroscopic ellipsometry of epitaxial ZnO layer on sapphire substrate, *J. Appl. Phys.* 87 (2000) 7820.
- [115] X.-Y. Gao, H.-L. Feng, J.-M. Ma, Z.-Y. Zhang, J.-X. Lu, Y.-S. Chen, et al., Analysis of the dielectric constants of the Ag₂O film by spectroscopic ellipsometry and single-oscillator model, *Physica B* 405 (2010) 1922–1926.
- [116] H. Kumagai, M. Matsumoto, K. Toyoda, M. Obara, Preparation and characteristics of nickel oxide thin film by controlled growth with sequential surface chemical reactions, *J. Mater. Sci. Lett.* 15 (1996) 1081–1083.
- [117] J.G. Endriz, W.E. Spicer, Reflectance studies of Ba, Sr, Eu, and Yb, *Phys. Rev. B* 2 (1970) 1466–1492.
- [118] R. Machorro, J.M. Siqueiros, S. Wang, Optical properties of Mg, from UV to IR, using ellipsometry and reflectometry, *Thin Solid Films* 269 (1995) 1–5.
- [119] L.I. Berger, Optical properties of selected inorganic and organic solids. *Handbook of Chemistry and Physics* 12_151–12_169.
- [120] R.A. May, L. Kondrachova, B.P. Hahn, K.J. Stevenson, Optical constants of electrodeposited mixed molybdenum–tungsten oxide films determined by variable-angle spectroscopic ellipsometry, *J. Phys. Chem. C* 111 (2007) 18251–18257.
- [121] R. Steim, F.R. Kogler, C.J. Brabec, Interface materials for organic solar cells, *J. Mater. Chem.* 20 (2010) 2499–2512.
- [122] O.S. Heavens, Optical properties of thin films, 2nd ed., Dover Publications, Mineola, NY, 2011.
- [123] N. Blouin, A. Michaud, M. Leclerc, A low-bandgap poly(2,7-carbazole) derivative for use in high-performance solar cells, *Adv. Mater.* 19 (2007) 2295–2300.
- [124] J. You, C.-C. Chen, L. Dou, S. Murase, H.-S. Duan, S.A. Hawks, et al., Metal oxide nanoparticles as an electron-transport layer in high-performance and stable inverted polymer solar cells, *Adv. Mater.* 24 (2012) 5267–5272.
- [125] P.R. West, S. Ishii, G.V. Naik, N.K. Emani, V.M. Shalae, A. Boltasseva, Searching for better plasmonic materials, *Laser Photonics Revs.* 4 (2010) 795–808.
- [126] J.D. Servaites, S. Yeganeh, T.J. Marks, M.A. Ratner, Efficiency enhancement in organic photovoltaic cells: consequences of optimizing series resistance, *Adv. Funct. Mater.* 20 (2010) 97–104.
- [127] P. Schilinsky, C. Waldauf, C.J. Brabec, Performance analysis of printed bulk heterojunction solar cells, *Adv. Funct. Mater.* 16 (2006) 1669–1672.